

**ARTICLE**

The Non-Singular Fast Terminal Sliding Mode Control of Interior Permanent Magnet Synchronous Motor Based on Deep Flux Weakening Switching Point Tracking

Xiangfei Li, Yang Yin, Yang Zhou, Wenchang Liu and Kaihui Zhao*

College of Electrical and Information Engineering, Hunan University of Technology, Zhuzhou, 412007, China

*Corresponding Author: Kaihui Zhao. Email: zhaokaihui@hut.edu.cn

Received: 10 March 2022 Accepted: 27 May 2022

ABSTRACT

This paper presents a novel non-singular fast terminal sliding mode control (NFTSMC) based on the deep flux weakening switching point tracking method in order to improve the control performance of permanent interior magnet synchronous motor (IPMSM) drive systems. The mathematical model of flux weakening (FW) control is established, and the deep flux weakening switching point is calculated accurately by analyzing the relationship between the torque curve and voltage decline curve. Next, a second-order NFTSMC is designed for the speed loop controller to ensure that the system converges to the equilibrium state in finite time. Then, an extended sliding mode disturbance observer (ESMDO) is designed to estimate the uncertainty of the system. Finally, compared with both the PI control and sliding mode control (SMC) by simulations and experiments with different working conditions, the method proposed has the merits of accelerating convergence, improving steady-state accuracy, and minimizing the current and torque pulsation.

KEYWORDS

Interior permanent magnet synchronous motor (IPMSM); flux weakening (FW) control; non-singular fast terminal sliding mode control (NFTSMC); extended sliding mode disturbance observer (ESMDO)

1 Introduction

Interior permanent magnet synchronous motor (IPMSM) has merits concerning simple structure, flux density and strong coercivity of neodymium-iron-boron permanent magnet [1]. IPMSM has a stronger load-carrying capacity than surface-mounted permanent magnet synchronous motor (SPMSM) because of the uneven air gap field distribution [2]. In addition, a wider speed range can be obtained by adopting the flux weakening (FW) control strategy. Thus, IPMSM is widely used in engineering fields such as aerospace, rail transit, and intelligent robots [3].

Common FW control strategies include the formula calculation method, lookup table (LUT), gradient descent, and negative d -axis current compensation [4]. The formula calculation method [5] is highly dependent on the motor parameters, and the control performance of the system decline in the case of system disturbance, such as parameter perturbation. The LUT method [6] completely depends on a large amount of experimental data, and it is not universally applicable for motors with different types and parameters. The current gradient descent method [7] analyzes the relationships between



torque change direction and the position relation of limited voltage circle to correct the current of the d - q axis. However, the steps of calculation are complicated and tedious. The negative d -axis current compensation method [8,9] is simple, and the control system has better robustness because it does not depend on the motor parameters. When the voltage inverter is saturated, FW control is completed by applying compensation to the d -axis current.

At present, the PI algorithm has become the mainstream method for FW control because of its simple algorithms and mature technology. The PI algorithm is a linear control method that is widely used in motor control. However, IPMSM is a nonlinear system with various uncertainties, such as internal disturbance caused by high-speed and unmodeled dynamic excitation caused by deepened coupling of the d - q current regulator, which may affect the control performance of the system [10]. Eliminating PI control disturbances is difficult due to its limitations, such as integral saturation, which is unsuitable for applying high-performance occasions [11].

Many advanced nonlinear control theories have been applied in IPMSM high-performance in recent years. For example, model predictive control (MPC) [12], optimize feedforward control [13], neural network control [14], and so on. A single MPC controller with a brand-new linearization method was designed to tackle the strong coupled nonlinear IPMSM mathematical model [12]. A novel modification of the optimal torque control for IPMSM was adopted to optimize the control performance with time-varying parameters [13]. A feedforward neural network controller was adopted to solve the finite control set model predictive control (FCS-MPC) [14]. To some extent, the above control algorithms [12–14] depend on the known mathematical model and the system's nominal model and can be considered model-based control theory. However, IPMSM is a complex, nonlinear and time-varying system that has unavoidable parameter perturbations that are difficult to be modeled and measured. Thus, the above algorithms have some limitations in engineering applications.

To reduce the dependence on motor parameters, sliding mode control (SMC) has become a hot topic vis-a-vis the FW control of IPMSM. An SMC controller was designed to replace the PI controller in the voltage closed-loop [15], which accelerates the dynamic adjustment rate when the voltage inverter is saturated and enhances the anti-disturbance ability of the control system. An SMC controller based on the anti-integral saturation regulator [16,17] not only enhances the system's robustness, but also improves the current tracking performance and inhibits the torque ripple. The SMC speed controller based on the new sliding mode reaching law [18,19] was adopted to optimize the sliding mode switching performance, weaken chattering and improve the control performance of the system. However, for conventional SMC, the convergence of the system error is exponential asymptotic, and it cannot converge to zero in finite time. Therefore, the key technologies in FW control research are how accelerating the convergence of speed, improve the steady-state control accuracy, and enhance the disturbance resistance of the control system.

This paper presents a novel NFTSMC method based on deep flux weakening switching point tracking. It achieves fast and accurate tracking of reference speed and improves the robustness of the IPMSM drive system. The main contributions of this paper are summarized as follows:

- i) This method that combines NFTSMC with FW control is presented to improve the speed response of the IPMSM in flux weakening region. It has the features of both NFTSMC and FW control. More specifically, while the FW control based on deep flux weakening switching point tracking expands the actual speed range, the NFTSMC based on extended sliding mode disturbance observer (ESMDO) accelerates speed convergence, improves steady-state accuracy, and minimizes the current pulsation and torque pulsation.

- ii) The mathematical model of MTPV control is simplified. The deep flux weakening switching point is obtained by analyzing the relationship between the torque and the voltage drop curves.
- iii) The NFTSMC speed controller is designed based on the input and the output, which reduces the dependence on motor parameters.
- iv) ESMDO estimates the unknown part of external disturbances. It is added to the input of the NFTSMC speed controller as a feedforward compensation item.

2 Mathematical Model of IPMSM

Ignoring stator core saturation, eddy current, and hysteresis loss, permanent rotor magnet without winding damping winding and mutual leakage inductance between stator windings, stator voltage equation of IPMSM in the d - q reference can be described as [20]:

$$\begin{cases} u_d = R_s i_d + L_d \frac{di_d}{dt} - \omega_e L_q i_q \\ u_q = R_s i_q + L_q \frac{di_q}{dt} + \omega_e (L_d i_d + \psi_f) \end{cases} \quad (1)$$

where i_d, i_q are d - q axis stator currents (A); u_d, u_q are d - q axis stator voltages (V); L_d, L_q are d - q axis stator inductance (H); ψ_f is permanent magnet flux linkage (Wb); R_s is stator resistance (Ω); ω_e is the electric angular velocity (rad/s).

In steady-state operation, the stator voltages can be approximately simplified as:

$$\begin{cases} u_d \approx -\omega_e L_q i_q \\ u_q \approx \omega_e (L_d i_d + \psi_f) \end{cases} \quad (2)$$

The motor operation should meet the following requirements:

$$\begin{cases} i_s = \sqrt{i_d^2 + i_q^2} \leq i_{\text{lim}} \\ u_s = \sqrt{u_d^2 + u_q^2} \leq u_{\text{lim}} \end{cases} \quad (3)$$

where i_s, u_s denote stator current and stator voltage; $i_{\text{lim}}, u_{\text{lim}}$ denote limited current and limited voltage.

FW control consists of three processes: maximum torque per ampere (MTPA) control, constant power control, and maximum torque per volt (MTPV) control.

Fig. 1 presents the d - q -axis current trajectory diagram of FW control.

2.1 Maximum Torque Per Ampere (MTPA) Control

When the actual motor speed is lower than the nominal speed, the current trajectory of MTPA runs along the curve OA in Fig. 1. The electromagnetic torque remains constant during motor acceleration. In the d - q reference, the equations of electromagnetic torque and stator current are [21]:

$$\begin{cases} T_e = \frac{3}{2} n_p [\psi_f + (L_d - L_q) i_d] i_q \\ i_s = \sqrt{i_d^2 + i_q^2} \end{cases} \quad (4)$$

Constructing Lagrange function from Eq. (4), the stator current of d - q axis can be obtained as [22]:

$$\begin{cases} i_d = \frac{-\psi_f + \sqrt{\psi_f^2 + 4(L_d - L_q)^2 i_q^2}}{2(L_d - L_q)} \\ i_q = \frac{\left(\frac{8T_e \psi_f}{3n_p}\right) + \sqrt{\left(\frac{8T_e \psi_f}{3n_p}\right)^2 - 4[\psi_f^2 - 4(L_d - L_q)^2] \left[\left(\frac{4T_e}{3n_p}\right)^2 - \psi_f^2\right]}}{2[\psi_f^2 - 4(L_d - L_q)^2]} \end{cases} \quad (5)$$

where n_p denotes the pole number (pairs); T_e denotes the electromagnetic torque (N · m).

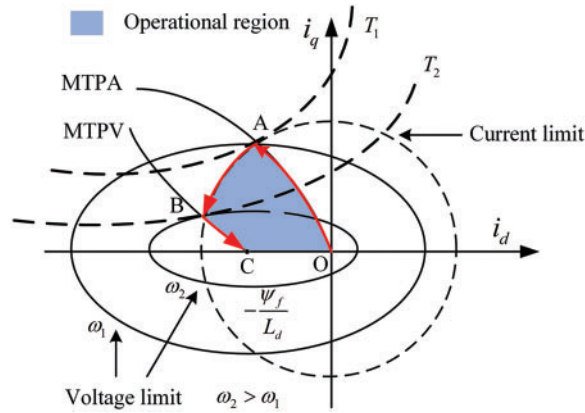


Figure 1: The d - q -axis current trajectory diagram of FW control

2.2 Maximum Torque Per Volt (MTPV) Control

The current trajectory in the shallow flux weakening region runs along with the curve AB in Fig. 1. The motor's actual speed is higher than the nominal speed, and the method of adding a negative d -axis current should be adopted to avoid saturation of the voltage inverter.

The current trajectory in the deep flux weakening region runs along the curve BC in Fig. 1. The MTPV control is suitable for the motor, which meets the requirement of $(\psi_f/L_d) < i_{im}$. Ideally, the motor speed can be further improved, but it cannot reach point C in practical applications. The current trajectory under control of MTPV is a curve connected by the limited voltage and the tangent points of the torque hyperbola. In other words, the line of the minimum voltage point is required to generate the maximum torque. The solution equation is:

$$\frac{\partial T_e}{\partial i_d} \cdot \frac{\partial u_s}{\partial i_q} - \frac{\partial T_e}{\partial i_q} \cdot \frac{\partial u_s}{\partial i_d} = 0 \quad (6)$$

Substituting Eqs. (2)–(4) into Eq. (6) yields

$$L_d^2 (L_d - L_q) i_d^2 + \psi_f L_d (2L_d - L_q) i_d + L_d \psi_f^2 - (L_d - L_q) L_q^2 i_q^2 = 0 \quad (7)$$

The expression of the d -axis current can be obtained as:

$$i_d = -\frac{\psi_f}{L_d} + \frac{-\psi_f L_q + \sqrt{L_q^2 \psi_f^2 + 4L_d^2 (L_d - L_q)^2 i_q^2}}{2L_d^2 (L_d - L_q)} \quad (8)$$

3 Optimization of Deep Flux Weakening Control

3.1 Negative D -Axis Current Compensated Method

When the motor is running, the saturation of the output voltage of the inverter is judged by constructing a voltage closed-loop. When $u_s \leq u_{dc}/\sqrt{3}$, voltage inverter is not saturated and the current compensation value of the d -axis is 0. When $u_s > u_{dc}/\sqrt{3}$, the voltage inverter is saturated. From Eq. (2), the d -axis current should be compensated by the saturation degree of the inverter so that the actual output voltage is less than the limited voltage. The regulating ability of the current regulator can be restored, and the motor can operate normally in the constant power region by taking the above measures. From Eq. (3), the compensation value can be expressed as:

$$\begin{cases} \sqrt{u_d^2 + u_q^2} \leq u_{dc}/\sqrt{3}, i_{dm} = 0 \\ \sqrt{u_d^2 + u_q^2} \geq u_{dc}/\sqrt{3}, i_{dm} < 0 \end{cases} \quad (9)$$

where i_{dm} is the value of d -axis current, which is output by PI.

3.2 The Principle of Determination of Deep Flux Weakening Switching Point

The conventional d -axis negative compensation method usually sets point E ($i_{d_set} = -\psi_f/L_d$) as the switching point. Fig. 2 presents the current trajectory diagram of negative d -axis current compensation.

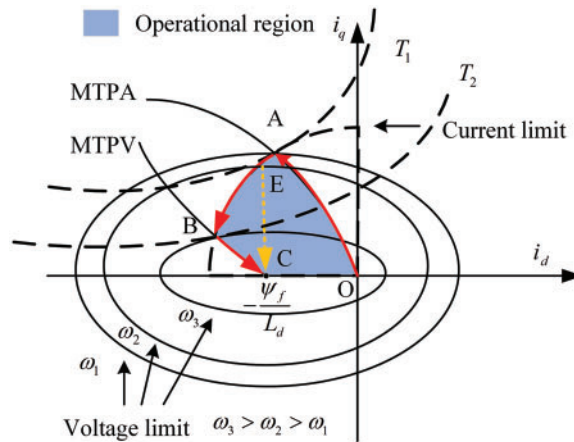


Figure 2: The d - q axis current trajectory diagram of negative d -axis current compensation

The current trajectory moves leftward from point A to point B. If setting point E as a switching point, the actual current cannot reach point B, resulting in a narrow speed regulation range. It can be seen from Fig. 2 that, in order to reach point B and expand the speed regulation range, the torque curve at point B is tangent to the limited voltage. From Eq. (2), ω_c is regarded as a constant coefficient, then the change curve of torque and the decline curve of fixed voltage can be considered as functions

of i_d and i_q . The deep flux weakening switching signal is constructed by calculating the angle between the direction of torque change and the direction of voltage drop.

According to Eq. (4), the direction of torque change is written in matrix form

$$\mathbf{T} = \begin{bmatrix} T_d \\ T_q \end{bmatrix} = \begin{bmatrix} \frac{\partial T_e}{\partial i_d} \\ -\frac{\partial T_e}{\partial i_q} \end{bmatrix} = \frac{3}{2} n_p \begin{bmatrix} L_d - L_q & 0 \\ 0 & L_q - L_d - \psi_f \end{bmatrix} \begin{bmatrix} i_q \\ i_d \end{bmatrix} \quad (10)$$

Substituting Eq. (2) into Eq. (3) yields

$$u_s^2 = (\omega_e L_q i_q)^2 + \omega_e^2 (L_d i_d + \psi_f)^2 \quad (11)$$

To obtain the decline direction of voltage, a new voltage change function is designed by i_d and i_q as:

$$F = (\omega_e L_q i_q)^2 + \omega_e^2 (L_d i_d + \psi_f)^2 \quad (12)$$

Combining Eqs. (2) and (12), the direction of voltages decline is written as a form of matrix

$$\mathbf{U} = \begin{bmatrix} U_d \\ U_q \end{bmatrix} = \begin{bmatrix} \frac{\partial F}{\partial i_d} \\ \frac{\partial F}{\partial i_q} \end{bmatrix} = \begin{bmatrix} 0 \\ \omega_e^2 L_d \psi_f \end{bmatrix} + \begin{bmatrix} 2(\omega_e L_d)^2 & 0 \\ 0 & 2(\omega_e L_q)^2 \end{bmatrix} \begin{bmatrix} i_d \\ i_q \end{bmatrix} \quad (13)$$

According to Eqs. (10) and (13), the switching signal is constructed as:

$$\cos \theta = \frac{\begin{bmatrix} T_d & T_q \end{bmatrix}^T \begin{bmatrix} U_d & U_q \end{bmatrix}}{\|\mathbf{T}\| \cdot \|\mathbf{U}\|} \quad (14)$$

where θ is the angle of torque change vector and voltage drop vector (rad). The state of flux weakening operation is determined by the value of θ [23]. When $\theta < \pi/2$ and $\cos \theta > 0$, the operation state of the motor is in the shallow flux weakening region; When $\theta > \pi/2$ and $\cos \theta < 0$, the operation state of the motor is in the deep flux weakening region. With the increase of speed, the value of θ increases gradually and $\cos \theta$ decreases continuously. When θ increases to $\pi/2$ and $\cos \theta$ decreases to 0, the switching point between shallow and deep flux weakening is obtained. At this time, the torque change vector and voltage drop vector are perpendicular to each other; furthermore, the motor's operation state switches from constant power FW control to MTPV control. Since the d -axis current cannot continue to decrease, the reference q -axis current can be reduced to obtain a higher speed.

$$\begin{cases} \cos \theta > 0, i_{qm} = 0 \\ \cos \theta < 0, i_{qm} < 0 \end{cases} \quad (15)$$

The q -axis current can be designed as

$$i_q = i_{qo} + i_{qm} \quad (16)$$

To further simplify the control algorithm, the relationship between compensation value of q -axis current and i_{dm} is designed as [24]:

$$\begin{cases} i_{qm} = \varepsilon (i_{do} + i_{dm} - i_{d_set}) \\ \varepsilon = \frac{L_d \psi_d}{L_q \psi_q} \end{cases} \quad (17)$$

where ε is the gain of compensation correction for q -axis current. Substituting Eq. (17) into Eq. (16) and combining Eq. (8), the reference d - q axis current in the deep flux weakening region can be designed as:

$$\begin{cases} i_q = i_{qo} + \frac{L_d \psi_d}{L_q \psi_q} (i_{do} + i_{dm} - i_{d_set}) \\ i_d = -\frac{\psi_f}{L_d} + \frac{-\psi_f L_q + \sqrt{L_q^2 \psi_f^2 + 4L_d^2 (L_d - L_q)^2 i_q^2}}{2L_d^2 (L_d - L_q)} \end{cases} \quad (18)$$

where i_{do} presents the reference current of d -axis output by MTPA; i_{qo} presents the reference current of q -axis output by the speed controller. Fig. 3 shows FW control's block diagram is based on switching point tracking.

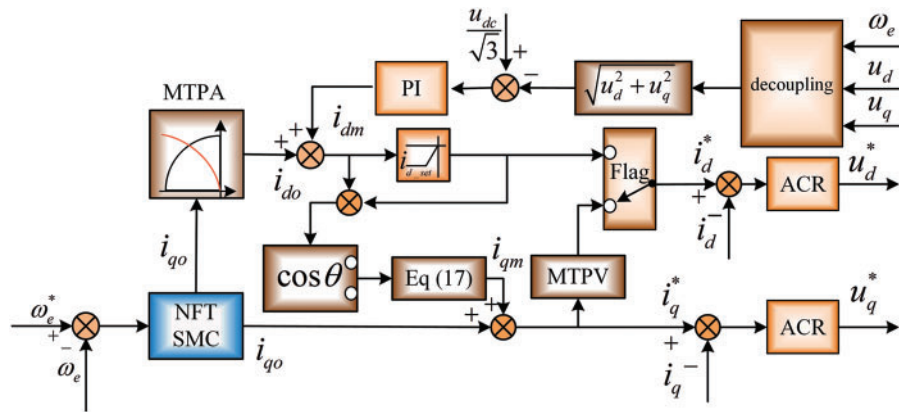


Figure 3: The block diagram of FW control

4 NFTSMC Speed Controller

To avoid integral saturation of PI and chattering problem of SMC, a second-order NFTSMC speed controller is designed to improve the performance of IPMSM, and an ESMDO is designed to estimate the unknown disturbances.

4.1 Designed of NFTSMC Speed Control

The equation of electromagnetic torque Eq. (4) can be described as:

$$T_e = \frac{3}{2} n_p [\psi_f + (L_d - L_q) i_d] i_q = \frac{3}{2} n_p \psi_{ext} i_q \quad (19)$$

where $\psi_{ext} = \psi_f + (L_d - L_q) i_d$ can be considered as active flux [25].

The mechanical motion equation of IPMSM is:

$$\frac{d\omega_e}{dt} = \frac{n_p}{J} (T_e - T_L - B\omega_m) \quad (20)$$

Substituting Eq. (19) into Eq. (20) yields

$$\frac{d\omega_e}{dt} = \frac{3n_p^2}{2J} \psi_{ext} i_q - \frac{B}{J} \omega_e - \frac{n_p}{J} T_L = \gamma i_q + \xi \omega_e + F \quad (21)$$

where T_L is load torque (N · m); J is a moment of inertia (kg · m²); B presents damping coefficient (N · m · s); ω_m is the mechanical angular velocity (rad/s); γ is the gain of q -axis stator current to be designed; $\xi = B/J$; $\gamma = 3n_p^2 \psi_{ext}/2J$; F is the total perturbation of uncertainty.

To accelerate speed transient response and improve steady-state control accuracy, an NFTSMC speed controller is designed. From Eq. (21), the control law of speed controller can be designed as:

$$\dot{i}_q^* = \frac{\dot{\omega}_e^* - \xi \omega_e - F + u_c}{\gamma} \quad (22)$$

where ω_e^* denotes the reference value of ω_e ; u_c is feedback control law of NFTSMC to be designed.

Substituting Eq. (21) into Eq. (22) yields

$$\dot{\omega}_e^* - \dot{\omega}_e + u_c = 0 \quad (23)$$

Define the state error of the controller as:

$$e = \omega_e^* - \omega_e \quad (24)$$

Then, the state variable is defined as $e_1 = e_2 = \omega_e^* - \omega_e$ and $\dot{e}_2 = \dot{e} = \dot{\omega}_e^* - \dot{\omega}_e$.

Selecting a second-order NFTSMC surface as below [26]:

$$s = e_1 + \alpha e_1^{g/h} + \beta e_2^{p/q} \quad (25)$$

where $\alpha > 0$; $\beta > 0$; g, h, p and q are positive odd numbers; $1 < p/q < 2$; $g/h > p/q$.

$$\begin{aligned} \dot{s} &= \dot{e}_1 + \alpha \frac{g}{h} e_1^{g/h-1} \dot{e}_1 + \beta \frac{p}{q} e_2^{p/q-1} \dot{e}_2 \\ &= \dot{e}_2 + \alpha \frac{g}{h} e_1^{g/h-1} \dot{e}_1 + \beta \frac{p}{q} e_2^{p/q-1} \dot{e}_2 \end{aligned} \quad (26)$$

Choose the exponential reaching law as:

$$\dot{s} = -\eta_1 \operatorname{sgn}(s) - \eta_2 s \quad (27)$$

where η_1 and η_2 are both positive numbers.

Theorem 1: For the rotational speed error Eq. (24), chosen Eq. (25) as the sliding mode surface and Eq. (27) as reaching law, then the system state will converge to zero in finite time.

From Eqs. (26) and (27), the feedback control law of the NFTSMC is obtained as below:

$$u_c = \frac{q}{\beta p} e_2^{2-p/q} \cdot \left(1 + \frac{\alpha g}{h} e_1^{g/h-1} \right) + \eta_1 \operatorname{sgn}(s) + \eta_2 s \quad (28)$$

Proof: Selecting Lyapunov function candidate to be

$$V = \frac{1}{2} s^2 \quad (29)$$

The derivative of V is:

$$\begin{aligned}
 \dot{V} &= s \left[e_2 + \alpha \frac{g}{h} e_1^{g/h-1} e_2 + \beta \frac{p}{q} e_2^{p/q-1} \dot{e} \right] \\
 &= s \left[e_2 + \alpha \frac{g}{h} e_1^{g/h-1} e_2 + \beta \frac{p}{q} e_2^{p/q-1} \cdot \left(-\eta_1 \text{sgn}(s) - \eta_2 s - \frac{q}{\beta p} e_2^{2-p/q} \left(1 + \frac{\alpha g}{h} e_1^{g/h-1} \right) \right) \right] \\
 &= s \left[e_2 + \alpha \frac{g}{h} e_1^{g/h-1} e_2 - e_2 \left(1 + \frac{\alpha g}{h} e_1^{g/h-1} \right) + \beta \frac{p}{q} e_2^{p/q-1} \left(\hat{F} - F - \eta_1 \text{sgn}(s) - \eta_2 s \right) \right] \\
 &= s \left[\beta \frac{p}{q} e_2^{p/q-1} \left(\|\tilde{F}\| - \eta_1 \text{sgn}(s) - \eta_2 s \right) \right] \\
 &\leq \beta \frac{p}{q} e_2^{p/q-1} \left(\left(\|\tilde{F}\| - \eta_1 \right) \|s\| - \eta_2 \|s\|^2 \right)
 \end{aligned} \tag{30}$$

Due to $1 < p/q < 2, 0 < p/q - 1 < 1, p > q, p$ and q are odd numbers, we can obtain $e_2^{p/q-1} > 0$. Due to β, η_1 and η_2 are positive numbers, chosen $\eta_1 \geq \|\tilde{F}\|$ yields Eq. (30) $\dot{V} \leq 0$.

It completes the proof.

Substituting Eq. (28) into Eq. (22), we can obtain the total control law i_q^* of the speed controller as:

$$i_q^* = \frac{\dot{\omega}_e^* - \xi \omega_e - F + \frac{q}{\beta p} e_2^{2-p/q} \cdot \left(1 + \frac{\alpha g}{h} e_1^{g/h-1} \right) + \eta_1 \text{sgn}(s) + \eta_2 s}{\gamma} \tag{31}$$

Fig. 4 presents the schematic diagram of the NFTSMC speed controller.

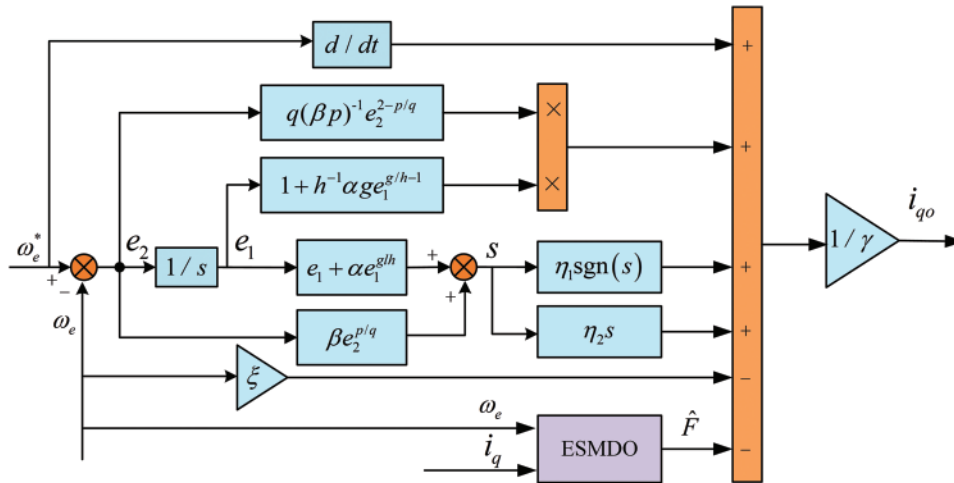


Figure 4: The schematic diagram of NFTSMC speed controller

4.2 Extended Sliding Mode Disturbance Observer

The ESMDO can estimate the uncertainty of the system by measuring the input and output of the actual system. It provides not only practical feasibility for the technical realization and practical applications in motor control. The variable is defined as $x = \hat{\omega}_e - \omega_e$, and Eq. (21) is redescribed as:

$$\begin{cases} \frac{d\hat{\omega}_e}{dt} = \gamma i_q + \xi \hat{\omega}_e + \hat{F} + u_{smo} \\ \frac{d\hat{F}}{dt} = G \cdot u_{smo} \end{cases} \quad (32)$$

where $\hat{\omega}_e$ is the observed value of ω_e ; \hat{F} is the estimated value of F ; $G > 0$ is the gain of sliding mode observer; u_{smo} is the control law of the sliding mode observer.

Combining Eqs. (21) and (32) obtains the equation:

$$\begin{cases} \dot{x} = \xi x + \tilde{F} + u_{smo} \\ \frac{d\tilde{F}}{dt} = G \cdot u_{smo} - \mathfrak{R}(t) \end{cases} \quad (33)$$

where $\tilde{F} = \hat{F} - F$; $\mathfrak{R}(t) = dF/dt$ is the rate of change for F .

Select the speed error as the sliding mode surface:

$$s_1 = x = \hat{\omega}_e - \omega_e \quad (34)$$

Choose the exponential reaching law as:

$$\dot{s}_1 = -\eta_3 \text{sgn}(x) - \eta_4 x \quad (35)$$

where $\eta_3 > 0$, $\eta_4 > 0$.

The control law of the sliding mode observer can be obtained from Eqs. (33) to (35):

$$u_{smo} = -\xi x - \eta_3 \text{sgn}(x) - \eta_4 x \quad (36)$$

Theorem 2: The error x converges to zero in finite time if one chooses Eq. (34) as the sliding mode surface, and the gain of ESMDO is designed as $\eta_3 \geq \|\tilde{F}\|$.

Proof: Selecting Lyapunov function candidate to be:

$$V_1 = \frac{1}{2} s_1^2 \quad (37)$$

The derivative of V_1 is:

$$\begin{aligned} \dot{V}_1 &= s_1 \dot{s}_1 = x (\xi x + \tilde{F} + u_{smo}) = x (\tilde{F} - \eta_3 \text{sgn}(x) - \eta_4 x) \\ &= x \tilde{F} - \eta_3 x \text{sgn}(x) - \eta_4 x^2 \leq x \tilde{F} - \eta_3 x \text{sgn}(x) \\ &\leq \|x\| (\|\tilde{F}\| - \eta_3) \end{aligned} \quad (38)$$

Chosen $\eta_3 \geq \|\tilde{F}\|$ yields $\dot{V}_1 \leq 0$.

It completes the proof.

Substituting Eq. (36) into Eq. (32), the total disturbance estimation expression is:

$$\hat{F} = G \int (-\xi x - \eta_3 \text{sgn}(x) - \eta_4 x) dt \quad (39)$$

Substituting Eq. (39) into Eq. (31) yields

$$\dot{i}_q^* = \frac{\hat{\omega}_e^* - \xi \omega_e - \hat{F} + \eta_1 \text{sgn}(s) + \eta_2 s + \frac{q}{\beta p} e_2^{2-p/q} \cdot \left(1 + \frac{\alpha g}{h} e_1^{g/h-1}\right)}{\gamma} \quad (40)$$

To weaken the chattering of the system due to the sgn function, the continuous saturation function $H(s)$ is used to replace the sign function, and its functional form is designed as follows [27]:

$$H(s) = \frac{s}{|s| + \sigma} \quad (41)$$

where $\sigma > 0$. Fig. 5 represents the block diagram of NFTSMC based on deep flux weakening switching point tracking of the IPMSM drive system.

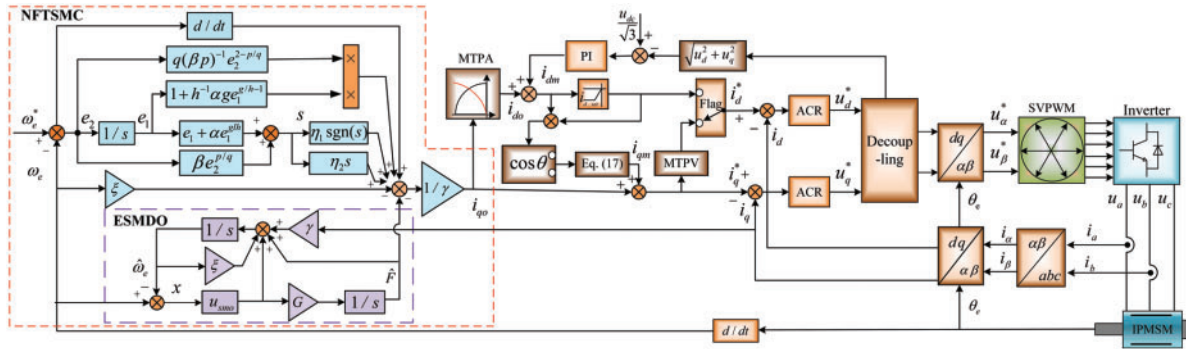


Figure 5: The block diagram of IPMSM drive system

5 Simulations and Experiments

To verify the feasibility and effectiveness of the proposed method, this section demonstrates the comparative analysis results of simulations and experiments.

5.1 Simulations Results

MATLAB/Simulink simulation is used to build a motor model compared with PI, conventional SMC, and NFTSMC. Table 1 represents the parameters of IPMSM. The drive system parameters of PI, SMC and NFTSMC are listed in Table 2.

Table 1: The parameters of IPMSM

Parameters	Unit	Values
Dc voltage/ u_{dc}	V	600
Rated speed/ n_N	r/min	1900
Stator resistance/ R_s	Ω	2.75

(Continued)

Table 1 (continued)

Parameters	Unit	Values
Pole number/ n_p	pairs	2
d axis inductance/ L_d	H	0.004
q axis inductance/ L_q	H	0.009
Magnetic flux/ ψ_f	Wb	0.12
Inertia/ J	$\text{kg} \cdot \text{m}^2$	0.029

Table 2: The parameters of control system

PI	SMC ¹	NFTSMC
$P = 100$	$c = 0.02$	$\alpha = 0.03$
$I = 10$	$k_1 = 2$	$\beta = 0.01$
/	$k_2 = 30$	$p/q = 7/5$
/	/	$g/h = 5/3$
/	/	$\eta_1 = 25$
/	/	$\eta_2 = 0.06$
/	/	$G = 200$
/	/	$\eta_3 = 2500$
/	/	$\eta_4 = 1.55$

Note: ¹The sliding mode surface and reaching law of SMC: $s = ce_1 + e_2$, $\dot{s} = -k_1 \text{sgn}(s) - k_2 s$.

Case 1: Graded speed regulation condition

The load torque is set as $T_L = 20 \text{ Nm}$, and the load torque is appropriately reduced to $T_L = 14 \text{ Nm}$ as the speed increases in the process of FW control operation. Settings of the motor are listed in [Table 3](#).

Table 3: Starting settings of motor

t/s	0	0.4	0.8	1.6
$n^*/(\text{r/min})$	1000	2000	4000	6000

[Figs. 6a–6c](#) demonstrate the simulation comparison results of speed, torque, and d - q axis current controlled by PI, SMC, and NFTSMC; [Figs. 6d](#) and [6e](#) show the observed value of $x = \hat{\omega}_e - \omega_e$ and the observed value of the total disturbances controlled by SMO and ESMDO.

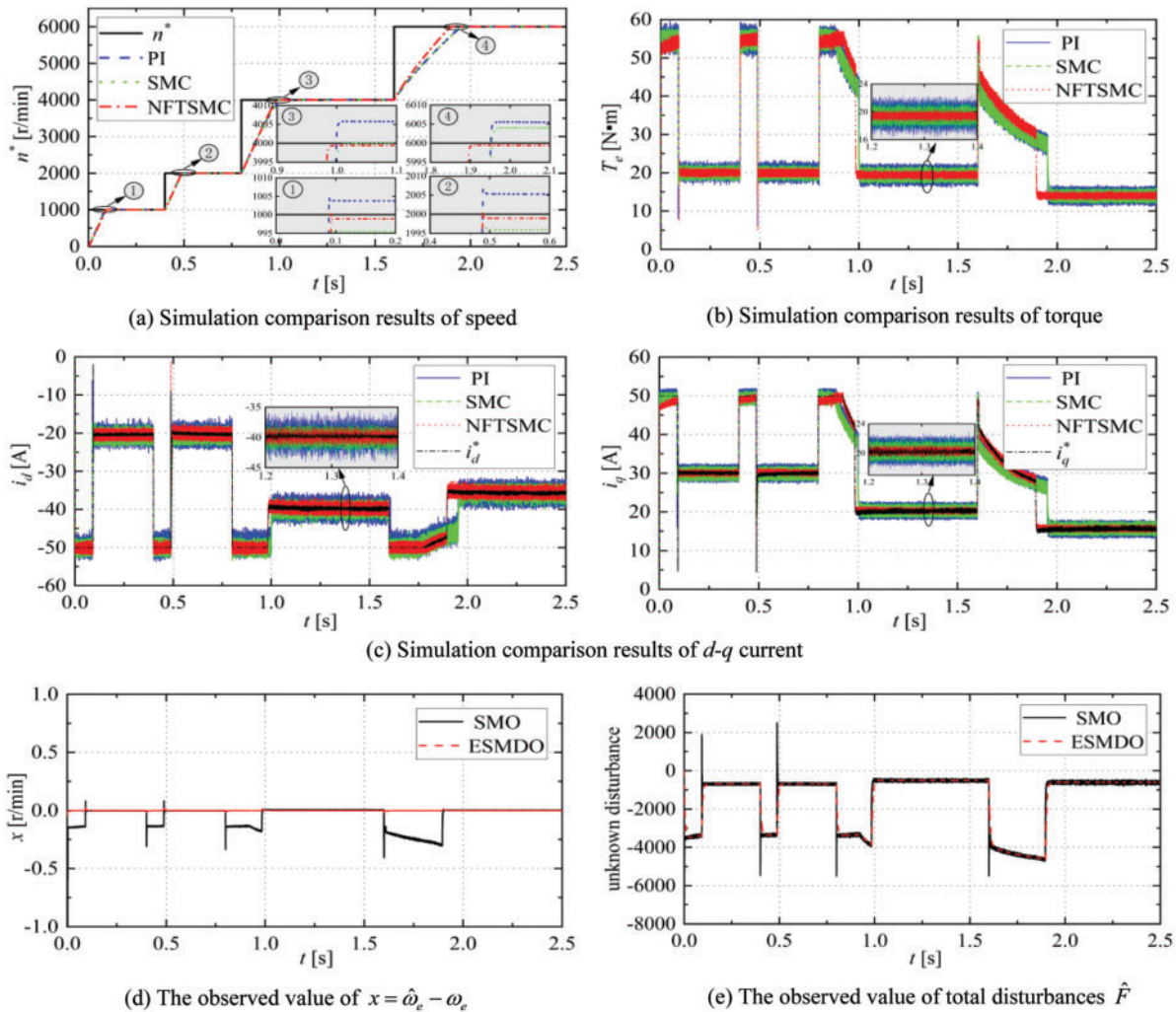


Figure 6: Simulation results of PI/SMC/ NFTSMC with graded speed regulation condition

The simulation comparison results are summarized in Table 4. For intuitive comparison, the comparison data of Table 4 is graphically processed to obtain Fig. 7.

Table 4: Steady state results of speed with PI/SMC/NFTSMC

$n^*/(\text{r}/\text{min})$	Convergence time/s	Speed relative error rate ¹ /%
1000	0.09/0.09/0.09	0.48/0.48/0.10
2000	0.49/0.49/0.49	0.27/0.22/0.05
4000	1.00/1.00/0.98	0.15/0.02/0.02
6000	1.96/1.96/1.90	0.10/0.08/0.01

Note: ¹Relative speed error rate represents the ratio of steady speed error amplitude of PI/SMC/NFTSMC to reference speed.

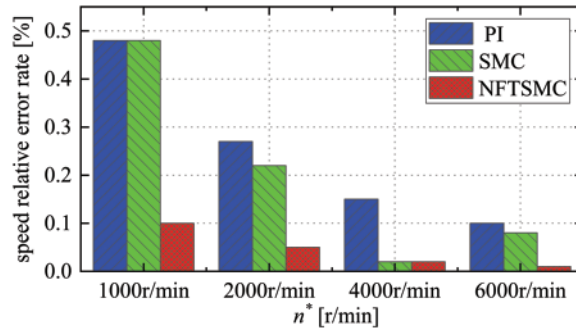


Figure 7: The comparison of speed relative error rate

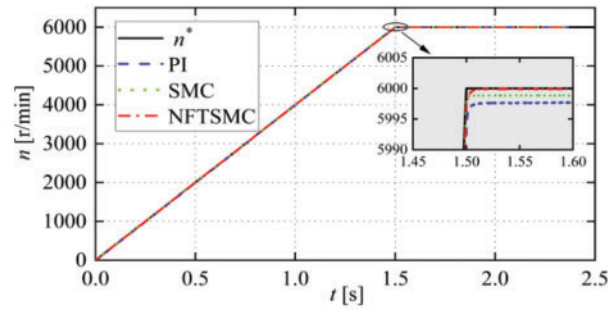
From Figs. 6a and 7, and Table 4, NFTSMC has better steady-state control accuracy than PI and SMC. When the reference speed changes from 2000 to 4000 r/min at 0.8 s, NFTSMC takes 0.18 s to reach steady-state, and the relative error rate of speed is only 0.02%. PI and SMC take 0.20 s to reach steady-state, and the relative error rate of speed are 0.15% and 0.02%. NFTSMC improves the dynamic response rate by 10%. When the reference speed changes from 4000 to 6000 r/min at 1.2 s, NFTSMC takes 0.3 s to reach reference speed, and the relative error rate of speed is only 0.01%. PI and SMC take 0.36 s to reach steady-state, and the relative error rate of speed is 0.10% and 0.08%. NFTSMC improves the dynamic response rate by 8%. In general, the NFTSMC speed controller can accelerate the dynamic convergence of speed in the flux weakening regions and further minimize the steady-state error of speed.

Figs. 6b and 6c demonstrate that the torque and d - q axis current waveform of NFTSMC are more stable, with smaller pulsation and better transient stability performance of the motor. It further shows that NFTSMC can effectively improve the control performance of the motor drive system.

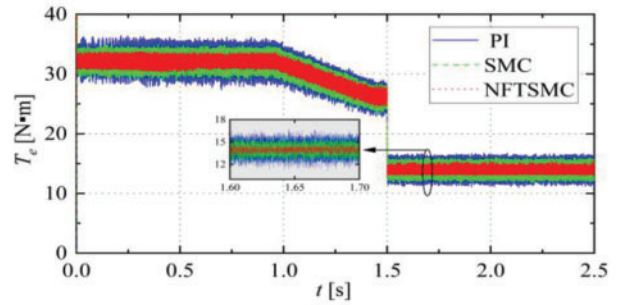
Figs. 6d and 6e demonstrate that the unknown disturbance and the speed observed by ESMDO is more accurate than that observed by SMO. This shows that the performance of ESMDO is better than SMO.

Case 2: Uniform acceleration condition

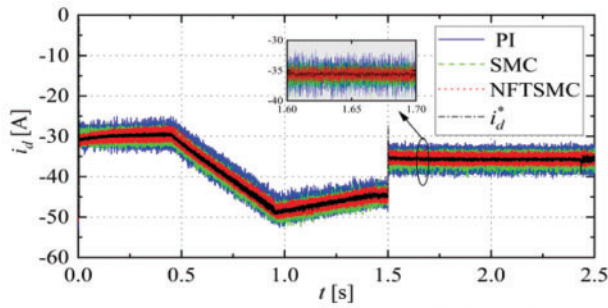
Setting the reference speed as a slope function to simulate uniform acceleration condition. Figs. 8a–8c demonstrate the simulation comparison of speed, torque, and d - q axis current controlled by PI, SMC, and NFTSMC; Figs. 8d and 8e show the observed value of $x = \hat{\omega}_e - \omega_e$ and the observed value of the total disturbances controlled by SMO and ESMDO. Figs. 8f–8h demonstrate the THD analysis of phase current. Fig. 8i demonstrates the d - q axis current trajectory. The comparison results of Fig. 8a are listed in Table 5.



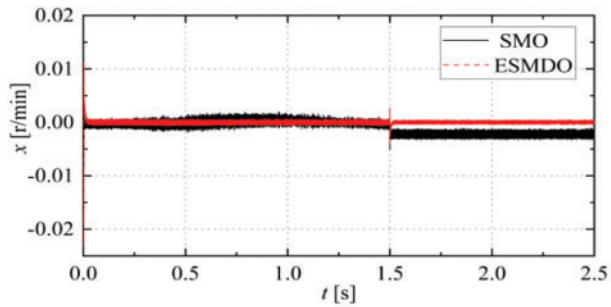
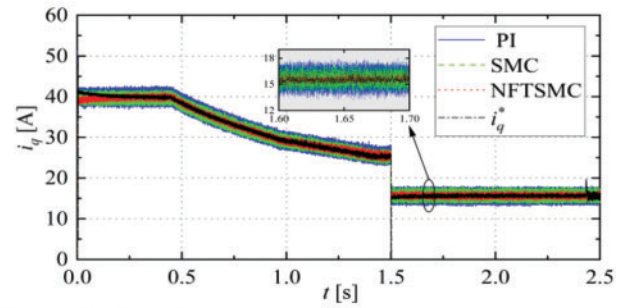
(a) Simulation comparison results of speed



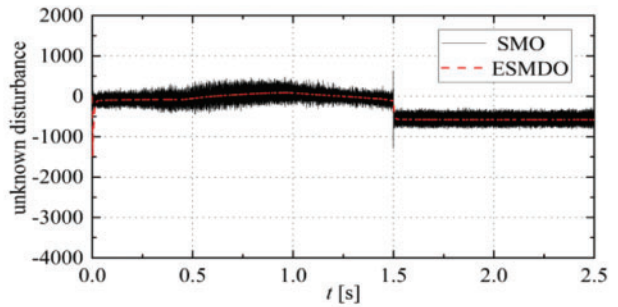
(b) Simulation comparison results of torque



(c) Simulation comparison results of current

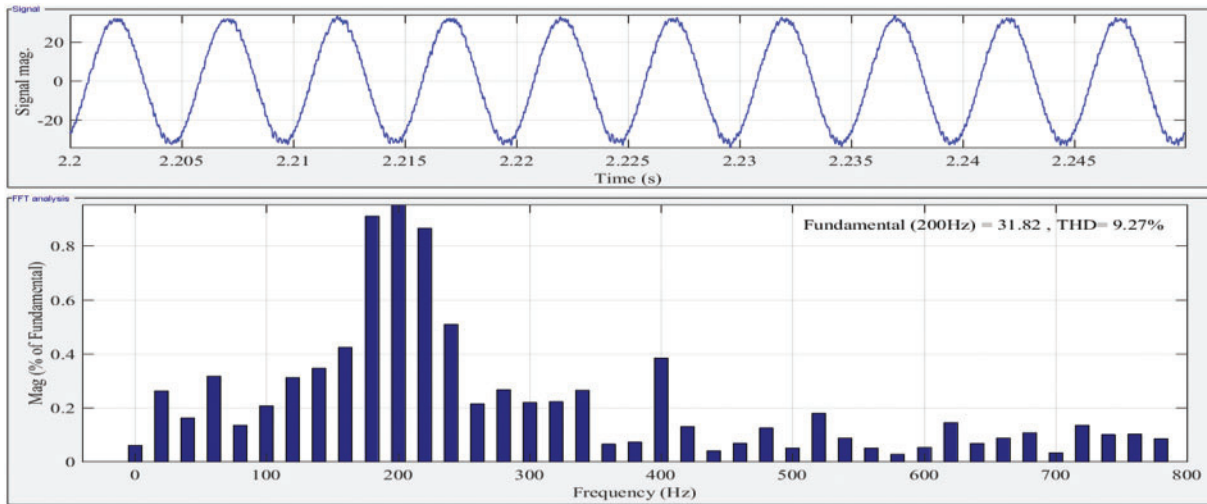


(d) The observed value of $x = \hat{\omega}_e - \omega_e$

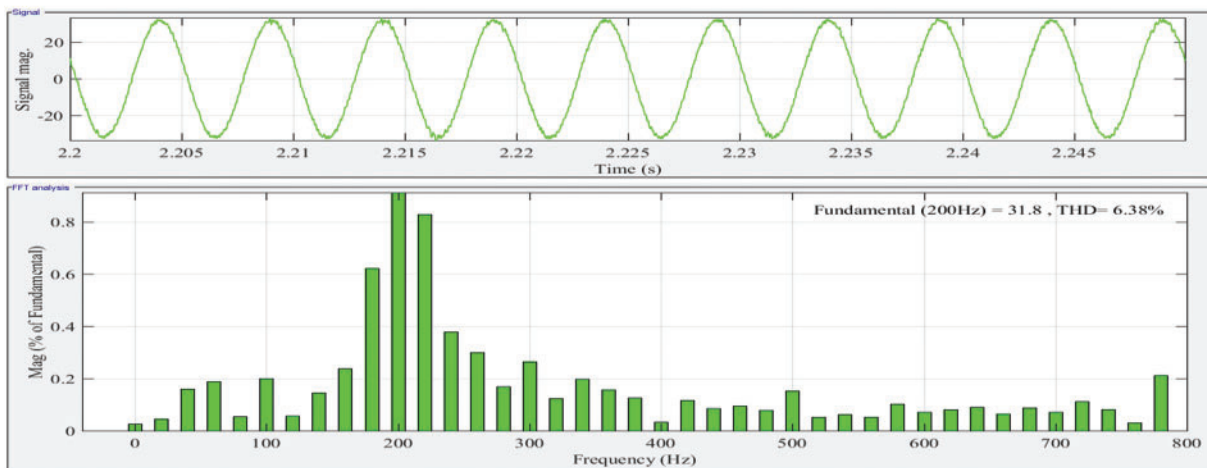


(e) The observed value of total disturbances \hat{F}

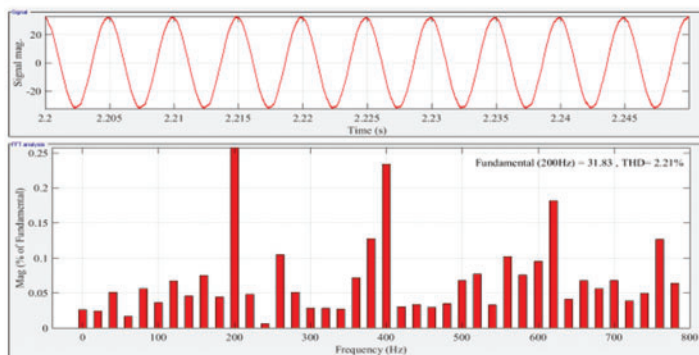
Figure 8: (Continued)



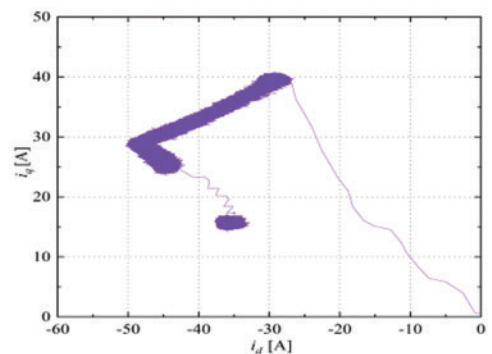
(f) The THD analysis of PI's phase current



(g) The THD analysis of SMC's phase current



(h) The THD analysis of NFTSMC's phase current



(i) The current trajectory of FW control

Figure 8: Simulation results of PI/SMC/NFTSMC with uniform acceleration condition

Table 5: Steady-state results of PI/SMC/NFTSMC

Convergence time/s	Speed relative error rate/%
1.50/1.50/1.50	0.03/0.018/0.001

From Fig. 8a and Table 5, there is no significant difference in the speed response rate of three methods with uniform acceleration, but the control accuracy of NFTSMC is significantly better than PI and SMC. Combined with Figs. 8a, 8d, and 8e, the unknown disturbances are estimated quickly by ESMDO to ensure that NFTSMC can effectively reduce chattering and improve the robustness of the drive system.

Figs. 8b and 8c demonstrate that the torque and current pulsation of PI are the largest and the convergence performance is the worst in the motor operation process. NFTSMC has the most stable d - q axis current and torque, and the pulsation of NFTSMC is the smallest. The simulation results show that the NFTSMC speed controller performs better transient steady-state control.

Fig. 8i demonstrates the current track diagram of NFTSMC. It is shown that the simulation current track conforms to the theoretical track of FW control. The d -axis current value of the deep flux weakening switching point is about -48A , far greater than the value of conventional settings, which verifies the correctness and effectiveness of the proposed method.

From Figs. 8f–8h, the THD value of phase current for PI is about 9.27%, and the THD value of phase current for SMC is about 6.38%. The THD value of phase current for NFTSMC is only 2.21%. The phase current of NFTSMC is much smoother. It means that the current harmonics of NFTSMC are smaller than PIs and SMCs. The comparison of THD analysis for phase current indicates that the drive system of NFTSMC has better control performance.

5.2 Experiments Results

To further test the effectiveness of the proposed method, the hardware-in-the-loop simulation (HILS) of IPMSM is carried out with DSP-TMS320F2812 and RT-Lab (OP5600) HILS platform. Fig. 9 shows the configuration diagram for the IPMSM drive systems.

Fig. 10 demonstrates the experimental results of PI, SMC and NFTSMC with graded speed regulation and uniform acceleration, respectively.

Compared with both Figs. 6 and 8, the control performance of the experiments is slightly decreased. Besides, the current pulsation and torque pulsation are more obvious in the transient condition, but the basic trend and effect comparison is consistent with the simulation results. As is shown in Fig. 10 and Table 6, the THD value of stator current for NFTSMC is the smallest. In addition, the average speed error rate of PI is 0.2%, and the average speed error rate of SMC is about 0.16%, while the average speed error rate of NFTSMC is only 0.04%. It indicates that NFTSMC has a better control accuracy. The torque ripple of PI is 20.0%, and the torque ripple of SMC is 15.0%, while the torque ripple of NFTSMC is only about 10.7% which is the smallest. The speed loop controller's current pulsation of q -axis output is the leading cause of the torque ripple. Because NFTSMC can accurately track the reference speed, the actual current pulsation of the d - q axis and torque pulsation is effectively minimized.

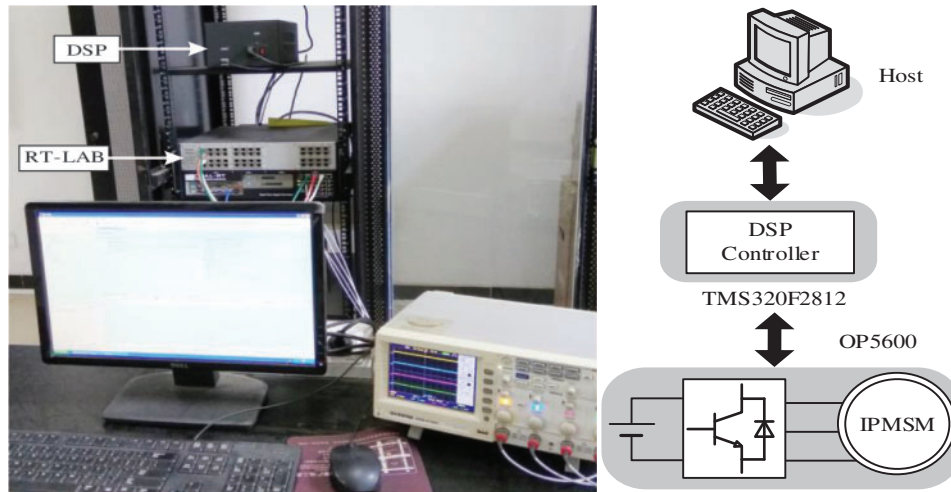
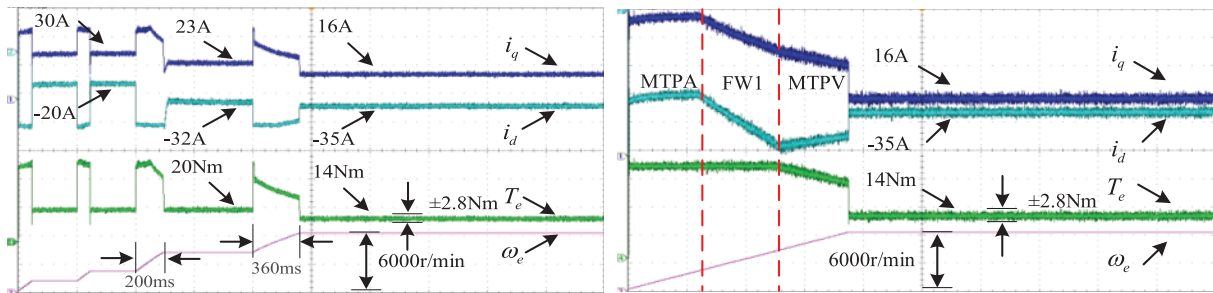
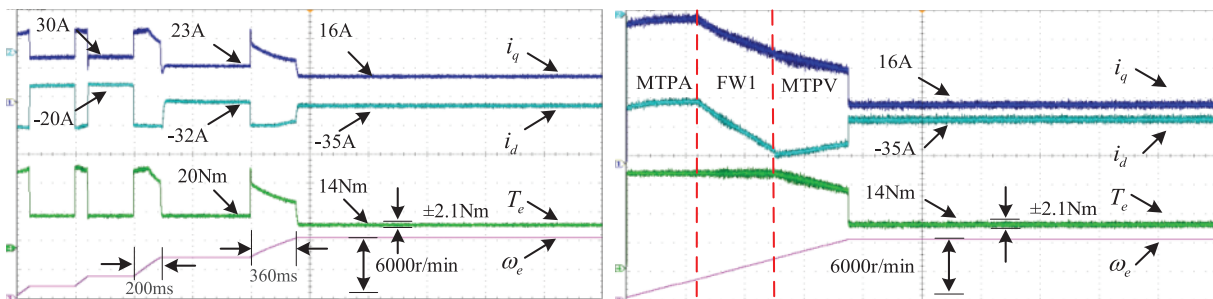


Figure 9: RT-Lab (OP5600) HILS experimental platform

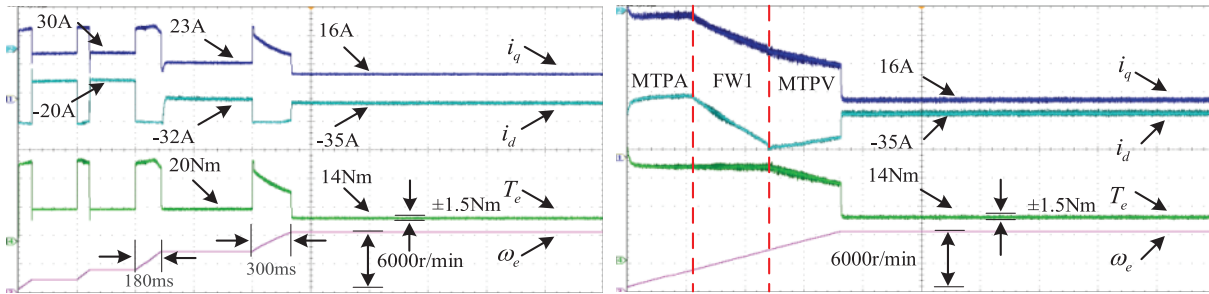


(a) The experimental results of PI



(b) The experimental results of SMC

Figure 10: (Continued)



(c) The experimental results of NFTSMC

Figure 10: The experimental results of PI/SMC/NFTSMC with different working conditions

Table 6: Comparison of PI/SMC/NFTSMC control methods

Performance indicators	PI	SMC	NFTSMC
Torque error /Nm	±2.8	±2.1	±1.5
Torque ripple ¹ /%	20.0	15.0	10.7
Average speed error rate ² /%	0.2	0.16	0.04
THD value of phase current/%	9.27	6.38	2.21

Notes: Torque ripple¹: The ratio of torque error amplitude to the reference torque. Average speed error rate²: The average speed relative error rate with different working conditions.

6 Conclusions

This paper presents a novel NFTSMC based on deep flux weakening switching point tracking of FW control for IPMSM drive system. The deep flux weakening switching point is accurately obtained, and the NFTSMC speed controller is designed based on the input and the output to accelerate speed convergence. The unknown part of external disturbances is estimated quickly by ESMDO, which is fed back to the NFTSMC speed controller. The comparative analysis results of simulations and experiments indicate that the method proposed has excellent speed response. In addition, it can effectively minimize the current and torque pulsation, and the IPMSM drive system has better transient steady-state performance.

Funding Statement: This work was partly supported by the Natural Science Foundation of China under Grant No. 61733004 and the Scientific Research Fund of the Hunan Provincial Education Department under Grand No. 18A267.

Conflicts of Interest: The authors declare that they have no conflicts of interest to report regarding the present study.

References

1. Tang, R. Y. (2016). *Modern permanent magnet machines: Theory and design*. China: China Machine Press.
2. Wei, Y. H., Luo, X., Zhu, L., Zhao, J. (2021). Research on current harmonic suppression strategy of high saliency ratio permanent magnet synchronous motor based on proportional resonance controller. *Proceedings of the CSEE*, 7, 2526–2538. DOI 10.13334/j.0258-8013.pcsee.200697.
3. Zhao, K. H., Zhang, C. F., He, J., Li, X. F., Feng, J. H. et al. (2017). Accurate torque-senseless control approach for interior permanent-magnet synchronous machine based on cascaded sliding mode observer. *Journal of Engineering*, 2017(7), 376–384. DOI 10.1049/joe.2017.0160.
4. Chen, Y. Z., Huang, X. Y., Wang, J., Niu, F., Zhang, J. et al. (2018). Improved flux-weakening control of IPMSMs based on torque feedforward technique. *IEEE Transactions on Power Electronics*, 33(12), 10970–10978. DOI 10.1109/TPEL.2018.2810862.
5. Pan, C. T., Sue, S. M. (2005). A linear maximum torque per ampere control for IPMSM drives over full-speed range. *IEEE Transactions on Energy Conversion*, 20(2), 359–366. DOI 10.1109/TEC.2004.841517.
6. Carlos, M. E., Daniel, H. P., Gabriel, G., Marc, L. M., Daniel, M. M. (2020). Maximum Torque per Voltage Flux-Weakening strategy with speed limiter for PMSM drives. *IEEE Transactions on Industrial Electronics*, 68(10), 9254–9264. DOI 10.1109/TIE.2020.3020029.
7. Li, K., Gu, X., Liu, X. D., Zhang, C. H. (2016). Optimized flux weakening control of IPMSM based on gradient descent method with single current regulator. *Transactions of China Electrotechnical Society*, 31(15), 8–15. DOI 10.19595/j.cnki.1000-6753.tces.2016.15.002.
8. Lin, F. J., Liao, Y. H., Lin, J. R., Lin, W. T. (2021). Interior permanent magnet synchronous motor drive system with machine learning-based maximum torque per ampere and flux-weakening control. *Energies*, 10(2), 346. DOI 10.3390/en14020346.
9. Zhang, Z. S., Wang, C. C., Zhou, M. L. (2020). Parameters compensation of permanent magnet synchronous motor in flux-weakening region for rail transit. *IEEE Transactions on Power Electronics*, 35(11), 12509–12521. DOI 10.1109/TPEL.2020.2987030.
10. Xia, C. Y., Sadiq, U. R., Liu, Y. (2020). Inter-turn fault diagnosis of permanent magnet synchronous machine considering model predictive control. *Proceedings of the CSEE*, 40(S1), 303–312. DOI 10.13334/j.0258-8013.pcsee.191394.
11. Zhao, K. H., Dai, W. K., Zhou, R. R., Leng, A. J., Liu, W. C. et al. (2022). Novel model-free sliding mode control of permanent magnet synchronous motor based on extended sliding mode disturbance observer. *Proceedings of the CSEE*, 42(6), 2375–2386. DOI 10.13334/j.0258-8013.pcsee.210273.
12. Liu, J. H., Gong, C., Han, Z. X., Yu, H. Z. (2018). IPMSM model predictive control in flux-weakening operation using an improved algorithm. *IEEE Transactions on Industrial Electronics*, 65(12), 9378–9387. DOI 10.1109/TIE.2018.2818640.
13. Glac, A., Šmídl, V., Peroutka, Z. (2018). Optimal feedforward torque control of synchronous machines with time-varying parameters. *44th Annual Conference of the IEEE Industrial Electronics Society*, pp. 613–618. Washington DC, USA, IEEE. DOI 10.1109/IECON.2018.8595139
14. Hammoud, I., Hentzelt, S., Oehlschlaegel, T., Kennel, R. (2020). Long-horizon direct model predictive control based on neural networks for electrical drives. *The 46th Annual Conference of the IEEE Industrial Electronics Society*, pp. 3057–3064. Singapore. DOI 10.1109/IECON43393.2020.9254388
15. Liu, G. H., He, F. Y., Wu, X., Wang, Y. (2018). Flux weakening control of interior permanent magnet synchronous motor based on slide mode controller. *Power Electronics*, 52(3), 82–85.
16. Akhil, R. S., Mini, V. P., Mayadevi, N., Harikumar, R. (2020). Modified flux-weakening control for electric vehicle with PMSM drive. *IFAC PapersOnLine*, 53(1), 325–331. DOI 10.1016/j.ifacol.2020.06.055.
17. Elena, T., Edorta, I., Antoni, A., Iñigo, K., Jonathan, J. et al. (2017). PM-assisted synchronous reluctance machine flux weakening control for EV and HEV applications. *IEEE Transactions on Industrial Electronics*, 65(4), 2986–2995. DOI 10.1109/TIE.2017.2748047.

18. Zhao, Y., Liu, B. (2017). Flux-weakening vector control of interior permanent magnet synchronous motor based on sliding mode variable structure controller. *Information and Control*, 46(4), 428–436 442. DOI 10.13976/j.cnki.xk.2017.0428.
19. Liu, B., Zhao, Y., Hu, H. Z. (2018). Structure-variable sliding mode control of interior permanent magnet synchronous motor in electric vehicles with improved flux-weakening method. *Advances in Mechanical Engineering*, 10(1), 168781401770435. DOI 10.1177/1687814017704355.
20. Zhao, K. H., Yin, T. H., Zhang, C. F., He, J., Li, X. F. et al. (2019). Robust model free nonsingular terminal sliding mode control of PMSM demagnetization fault. *IEEE Access*, 7, 15737–15748. DOI 10.1109/ACCESS.2019.2895512.
21. Li, K., Wang, Y. (2019). Maximum torque per ampere (MTPA) control for IPMSM drives using signal injection and an MTPA control law. *IEEE Transactions on Industrial Informatics*, 15(10), 5588–5598. DOI 10.1109/TII.2019.2905929.
22. Shi, M., Feng, J. H., Xu, J. F., He, Y. P., Xiao, L. (2015). Research of permanent magnet synchronous motor control stability improving in depth flux-weakening area. *Electric Drive for Locomotives*, 1, 22–25. DOI 10.13890/j.issn.1000-128x.2015.01.006.
23. Sheng, Y. F., Yu, S. Y., Gui, W. H., Gong, Z. N. (2010). Field weakening operation control strategies of permanent magnet synchronous motor for railway vehicle. *Proceedings of the CSEE*, 30(9), 74–79. DOI 10.13334/j.0258-8013.pcsee.2010.09.009.
24. Zhu, L. D., Wang, X., Zhu, H. Q. (2020). An IPMSM deep flux weakening algorithm with calculable parameters to avoid out-of-control. *Proceedings of the CSEE*, 40(10), 3328–3336. DOI 10.13334/j.0258-8013.pcsee.190945.
25. Wang, Y. Q., Zhu, Y. C., Feng, Y. T., Tian, B. (2021). New reaching law sliding-mode control strategy for permanent magnet synchronous motor. *Electric Power Automation Equipment*, 41(1), 192–198. DOI 10.16081/j.epae.202010005.
26. Xu, B., Zhang, L., Ji, W. (2021). Improved non-singular fast terminal sliding mode control with disturbance observer for PMSM drives. *IEEE Transactions on Transportation Electrification*, 7(4), 2753–2762. DOI 10.1109/TTE.2021.3083925.
27. Zhao, K. H., Liu, W. C., Yin, T. H., Zhou, R. R., Dai, W. K. et al. (2021). Model-free sliding mode control for PMSM drive system based on ultra-local model. *Energy Engineering*, 119(2), 767–780. DOI 10.32604/EE.2021.018617.